
Article:
Peng, C, Wu, W, Yu, H-S et al. (1 more author) (2015) A SPH approach for large deformation analysis with hypoplastic constitutive model. Acta Geotechnica, 10 (6). pp. 703-717. ISSN 1861-1125

https://doi.org/10.1007/s11440-015-0399-3

A SPH approach for large deformation analysis with hypoplastic constitutive model

Chong Peng[a,b], Wei Wu[b], Hai-sui Yu[a], Chun Wang[c]

[a] *Nottingham Center for Geomechanics, University of Nottingham, NG7 2RD, Nottingham, UK*
[b] *Institut für Geotechnik, Universität für Bodenkultur, Feistmantelstrasse 4, A-1180, Vienna, Austria*
[c] *School of Naval Architecture, Ocean and Civil Engineering, Shanghai Jiao Tong University, 200240, Shanghai, China*

Abstract

A hypoplastic constitutive model is implemented in a Smoothed Particle Hydrodynamics (SPH) code for the first time. An improved wall boundary treatment is presented for better performance. The proposed approach is first validated by comparing the numerical results with the analytical solutions for oedometer test. Two more problems involving large deformation, i.e. the collapse of sand between two parallel plates and the failure of a homogeneous slope, are analyzed to demonstrate the performance of the proposed method.

Keywords: Smoothed particle hydrodynamics, Large deformation, Hypoplastic constitutive model, Boundary conditions, Slope failure

1. Introduction

The simulation of problems involving large deformations and moving boundary conditions in geotechnical engineering has attracted much attention in recent years. The finite element method (FEM) is the most widely used numerical tool in computational geomechanics. However, the conventional FEM often gives rise to severe mesh distortion for problems with large deformation. Alternative approaches based on the FEM, such as Updated Lagrangian (UL) [1] and Arbitrary Eulerian-Lagrangian (AEL) [2, 3] have been developed, where re-meshing is usually required. The re-meshing, however, is not only difficult to implement in three dimensional simulations with complex and moving boundary conditions, but also introduces numerical errors due to the imperative interpolations between old and new meshes [3].

In the last two decades, numerous mesh-free methods have been proposed, which need no mesh in computation thus bear advantages compared to the traditional FEM in applications such as crack simulation [4, 5], shear band [6] and large deformation analysis [7]. Among them, the Smoothed Particle Hydrodynamics (SPH) is a well-established method and has a long application history in astrophysics [8, 9] and computational fluid dynamics (CFD) [10, 11, 12]. SPH is a pure Lagrangian method, where the material is described by a set of particles carrying field variables (e.g. position, mass, density, velocity, stress and strain) and moving with the material velocity. Because there is no mesh, through an updated Lagrangian scheme, SPH can

handle large deformation and complex material interface naturally. Besides applications in astrophysics and CFD, SPH has also been applied to solid problems such as dynamic response [13], impact [14] and explosion simulations [15].

In order to apply SPH to geomechanics problems, an appropriate constitutive model for the mechanical behavior of geomaterials is needed. In the conventional SPH, the pressure (stress) is computed form the density variation using an equation of state [10]. Although this treatment yields satisfactory results for fluid, it is obviously oversimplified for geomaterials. Some simplified models such as depth integration method [16] and Bingham fluid model [17] have been employed to simulate geophysical flows like lava and debris flow. However, these simplified models are still largely based on the approach of fluid mechanics. Bui and his co-workers implemented an elastoplastic constitutive model for soil with Drucker-Prager yield function within the framework of SPH [18, 19, 20]. Chen and Qiu [21] analyzed the collapse of a column of cohesionless granular material with a SPH code. Recently, SPH has been employed to simulate the interactions between soil and structures by Wang and Chan [22]. The constitutive models for soils in SPH give rise to more realistic and accurate simulation results for geomechanical problems [18].

In soil mechanics constitutive models are usually based on the decomposition of strain into elastic part and plastic part. On the other hand, hypoplastic constitutive models have been developed [23, 24, 25]. In the hypoplastic models, the stress rates are a non-linear function of strain rates. Unlike elastoplastic models, the hypoplastic models are formulated without recourse to such concepts as strain decomposition, yield surface, plastic potential or flow rule. Some of these concepts turn out as natural outcomes of the model [26], indicating that these well established concepts in soil mechanics can be unified in hypoplasticity. The formulations of most hypoplastic models are quite simple, and usually have fewer parameters. Despite the simplicity, however, hypoplastic models are capable of capturing some salient behaviors of soils [27]. Hypoplasticity is well established for both sand [27, 28] and clay [29], and has been applied to boundary value problems [30, 31, 32, 33]. Furthermore, hypoplastic constitutive equations are usually in rate form, which is a desirable feature for the implementation in SPH.

In this paper, a hypoplastic constitutive model presented by Wang [34] is employed in the SPH to simulate large deformation problems. Following the framework by Bui et al [18], the strain rate is evaluated from the velocity field. The stress rate is computed directly using the hypoplastic constitutive model. Some issues of the numerical implementation such as artificial viscosity, boundary condition and explicit integration scheme are discussed, and an improved treatment for the wall boundary is presented to prevent particles from penetrating into the boundary. The proposed SPH approach is first validated by simulating an oedometer test, where the numerical results are compared with the analytical solutions. Then two more numerical examples involving large deformations, namely, the collapse of sand between two parallel plates and the failure of a homogeneous slope, are analyzed.

2. SPH formulations

In the SPH, the problem domain is represented by a set of particles which carry field variables and move with the material body. Therefore, physical problems can be solved by tracking the movements of the particles and the changes of the carried field variables.

2.1. SPH integral interpolation

The approximation of physical variables in SPH is based on integral interpolation, by which, a field function $f(\boldsymbol{x})$ at position $\boldsymbol{x} = (x, y, z)$ is approximated by

$$< f(\boldsymbol{x}) >= \int_{\Omega} f(\boldsymbol{x}')W(\boldsymbol{x} - \boldsymbol{x}', h)\mathrm{d}\Omega \tag{1}$$

where the integral is over domain Ω surrounding position $\boldsymbol{x}$, and $\mathrm{d}\Omega$ is the element of volume represented by $\boldsymbol{x}'$. W is a weighting function called kernel function, and h is the smoothing length, which determines the size of the support domain of the kernel function W. An applicable kernel function should satisfy several requirements, such as the normalization condition, the delta function property condition and the compact support condition [35]. Following these requirements, a number of kernel functions have been proposed and applied in SPH, among them the cubic spine function is probably the most popular one. In this work the cubic spine function is applied, with the following form

$$W = \alpha_C \begin{cases} 1 - 1.5q^2 + 0.75q^3 & 0 \leq q < 1 \\ 0.25(2 - q)^3 & 1 \leq q < 2 \\ 0 & q \geq 2 \end{cases} \tag{2}$$

in which α_D is a normalization factor whose value is $10/(7\pi h^2)$ in two dimensions and $1/(\pi h^3)$ in three dimensions. q is the normalized distance between $\boldsymbol{x}$ and $\boldsymbol{x}'$, defined as $q = r/h$ where r is the Euclidean distance. It can be found that by using the above kernel function the radius of the support domain Ω is $2h$.

The spatial derivatives of the field function can be obtained by replacing $f(\boldsymbol{x})$ with $\nabla f(\boldsymbol{x})$ in Eq. (1)

$$< \nabla f(\boldsymbol{x}) >= \int_{\Omega} \nabla f(\boldsymbol{x}')W(\boldsymbol{x} - \boldsymbol{x}', h)\mathrm{d}\Omega \tag{3}$$

Integrating by parts and applying the divergence theorem, it is obtained that

$$< \nabla f(\boldsymbol{x}) >= \int_{S} f(\boldsymbol{x}')W(\boldsymbol{x} - \boldsymbol{x}', h)\boldsymbol{n}\mathrm{d}S - \int_{\Omega} f(\boldsymbol{x}')\nabla_{\boldsymbol{x}'}W(\boldsymbol{x} - \boldsymbol{x}', h)\mathrm{d}\Omega \tag{4}$$

where $\boldsymbol{n}$ is a unit vector normal to the domain surface S, and the subscript $\boldsymbol{x}'$ in $\nabla_{\boldsymbol{x}'}$ indicates that the derivatives are evaluated at position $\boldsymbol{x}'$. Owing to the compact support condition, the kernel function W has zero value on the surface if the whole support domain is located within the problem domain. In that

case, the surface integration in Eq. (4) vanishes, thus the derivatives of the field function can be computed as follows

$$< \nabla f(\boldsymbol{x}) >= -\int_{\Omega} f(\boldsymbol{x}')\nabla_{\boldsymbol{x}'} W(\boldsymbol{x}-\boldsymbol{x}', h)\mathrm{d}\Omega \tag{5}$$

It is an advantage of SPH that the derivatives of the field function can be obtained from the function values and the derivatives of the kernel function. However, generally, the zero value condition of W in the surface integral of Eq. (4) cannot be satisfied if the support domain intersects with the boundary of problem domain. In that circumstance, the value of the surface integral in Eq. (4) is no longer zero. This phenomenon is called particle deficiency in SPH, which calls for appropriate treatment of boundary condition. The implementation of boundary conditions will be further discussed in Section 4.2.

As mentioned previously, in SPH the problem domain is represented by particles. The continuous forms of integral interpolation in Eq. (1) and Eq. (5) can be rewritten as summations of contributions from the particles in the support domain. Consequently, the SPH approximations of $f(\boldsymbol{x})$ and $\nabla f(\boldsymbol{x})$ at particle i are written as

$$f(\boldsymbol{x}_i) = \sum_{j=1}^{n} f(\boldsymbol{x}_j) W_{ij} m_j/\rho_j \tag{6}$$

$$\nabla f(\boldsymbol{x}_i) = \sum_{j=1}^{n} f(\boldsymbol{x}_j) \nabla_i W_{ij} m_j/\rho_j \tag{7}$$

where n is the number of particles within the support domain, and m_j/ρ_j denotes the volume of material represented by particle j. In the above two equations $W(\boldsymbol{x}_i - \boldsymbol{x}_j, h)$ is termed as W_{ij} and the relationship $\nabla_i W_{ij} = -\nabla_j W_{ij}$ is used. By applying the aforementioned procedure of particle approximation, the SPH formulations of partial deferential equations can be derived.

2.2. Discretization of governing equations

The governing equations of soils are continuity equation and momentum equation

$$\frac{\mathrm{d}\rho}{\mathrm{d}t} = -\frac{1}{\rho}\nabla \cdot \boldsymbol{v} \tag{8}$$

$$\frac{\mathrm{d}\boldsymbol{v}}{\mathrm{d}t} = \frac{1}{\rho}\nabla \cdot \boldsymbol{\sigma} + \boldsymbol{g} \tag{9}$$

where ρ is the soil density; $\boldsymbol{v}$ denotes the velocity, $\boldsymbol{\sigma}$ the stress tensor and $\boldsymbol{g}$ the acceleration caused by body force, e.g. gravity in most geotechnical problems. In this paper pore pressure in soil is not considered, hence the stress tensor here is effective stress tensor. Because the hypoplastic model applied in this study does not

involve density, the continuity equation can be removed from the governing equations [18]. It means that the density variation is not considered and the particle volume remains constant during simulation.

Considering the term $\nabla\boldsymbol{\sigma}/\rho$ in the momentum equation Eq. (9), following the treatment presented by Monaghan [8], a symmetric form of the stress gradient can be obtained

$$\frac{\nabla\cdot\boldsymbol{\sigma}}{\rho}=\nabla\cdot(\frac{\boldsymbol{\sigma}}{\rho})+\frac{\boldsymbol{\sigma}}{\rho^2}\nabla\rho \tag{10}$$

By applying Eq. (7) and the above equation to Eq. (9), the momentum equation of particle i becomes

$$\frac{\mathrm{d}\boldsymbol{v}_i}{\mathrm{d}t}=\sum_{j=1}^{n}(\frac{\boldsymbol{\sigma}_i}{\rho_i^2}+\frac{\boldsymbol{\sigma}_j}{\rho_j^2})\nabla_i W_{ij}m_j+\boldsymbol{g}_i \tag{11}$$

This formula is probably the most commonly used to compute accelerations in SPH, though there are other variations applied by researchers [13, 22].

3. Hypoplastic constitutive model in SPH

A constitutive equation is imperative to close the momentum equation, that is, we need to compute the stress tensors in Eq. (11). To this end, the stress tensor is usually divided into two parts, i.e. a hydrostatic pressure p and a deviatoric stress tensor $\boldsymbol{\sigma}^*$ [13, 36]. Usually, the hydrostatic pressure p is computed by an equation of state from density variation, while the shear stress is computed from a constitutive equation [13]. In this work, we calculate the stress tensor directly from a constitutive equation without recourse to the equation of state. A simple hypoplastic constitutive model [34] is adapted to compute the stress rate from the velocity field.

3.1. Framework of hypoplasticity

In hypoplasticity, the stress rate is assumed to be a non-linear tensorial function of the strain rate and stress

$$\mathring{\boldsymbol{\sigma}}=\mathbf{H}(\boldsymbol{\sigma},\dot{\boldsymbol{\varepsilon}}) \tag{12}$$

where $\dot{\boldsymbol{\varepsilon}}$ is the strain rate tensor defined as $\dot{\boldsymbol{\varepsilon}}=\frac{1}{2}[(\nabla\boldsymbol{v})+(\nabla\boldsymbol{v})^{\mathrm{T}}]$, and $\mathring{\boldsymbol{\sigma}}$ is the Jaumann stress rate used for the sake of objectivity, which is defined by

$$\mathring{\boldsymbol{\sigma}}=\dot{\boldsymbol{\sigma}}+\boldsymbol{\sigma}\dot{\boldsymbol{\omega}}-\dot{\boldsymbol{\omega}}\boldsymbol{\sigma} \tag{13}$$

in which $\dot{\boldsymbol{\sigma}}$ is the stress rate, and $\dot{\boldsymbol{\omega}}$ is the spin tensor defined as $\dot{\boldsymbol{\omega}}=\frac{1}{2}[(\nabla\boldsymbol{v})-(\nabla\boldsymbol{v})^{\mathrm{T}}]$. Compression is taken to be negative in this paper.

In hypoplasticity, the constitutive equation (12) is written in two parts, representing respectively reversible and irreversible behaviors of soils. Different formulations for $\mathbf{H}(\boldsymbol{\sigma}, \dot{\boldsymbol{\varepsilon}})$ can be found in literature [25, 29]. The following expression has been used to define a class of rate-independent hypoplastic constitutive models [37]

$$\mathring{\boldsymbol{\sigma}} = \mathbf{H}(\boldsymbol{\sigma}, \dot{\boldsymbol{\varepsilon}}) = \mathbf{L}(\boldsymbol{\sigma}) : \dot{\boldsymbol{\varepsilon}} - \mathbf{N}(\boldsymbol{\sigma}) \parallel \dot{\boldsymbol{\varepsilon}} \parallel \tag{14}$$

where $\mathbf{L}(\boldsymbol{\sigma})$ and $\mathbf{N}(\boldsymbol{\sigma})$ are tensor functions resulting respectively a fourth order tensor and a second order tensor; $\parallel \dot{\boldsymbol{\varepsilon}} \parallel = \sqrt{\mathrm{tr}\dot{\boldsymbol{\varepsilon}}^2}$ is the Euclidean norm; the colon : denotes an inner product between two tensors. Usually $\mathbf{L}$ and $\mathbf{N}$ are constructed by picking out terms from the representation theorem for isotropic tensorial functions [38]. Owing to the non-differentiable term containing $\parallel \dot{\boldsymbol{\varepsilon}} \parallel$, the constitutive equation (14) is incrementally non-linear. Concepts like failure surface and flow rule can be derived from the constitutive equation (14), for details please refer to Wu and Niemunis (1996) [26].

3.2. A simple hypoplastic constitutive equation

In this paper the following specific hypoplastic constitutive equation [34], which is an improvement based on the constitutive equation proposed by Wu and Bauer [27], is considered

$$\mathring{\boldsymbol{\sigma}} = c_1(\mathrm{tr}\boldsymbol{\sigma})\dot{\boldsymbol{\varepsilon}} + c_2(\mathrm{tr}\dot{\boldsymbol{\varepsilon}})\boldsymbol{\sigma} + c_3\frac{\mathrm{tr}(\boldsymbol{\sigma}\dot{\boldsymbol{\varepsilon}})}{\mathrm{tr}\boldsymbol{\sigma}}\boldsymbol{\sigma} + c_4(\boldsymbol{\sigma} + \boldsymbol{\sigma}^*) \parallel \dot{\boldsymbol{\varepsilon}} \parallel \tag{15}$$

where c_i $(i = 1, \ldots, 4)$ are dimensionless parameters; $\mathrm{tr}(\cdot)$ denotes the trace of a tensor; and $\boldsymbol{\sigma}^*$ stands for the deviatoric stress tensor, defined as

$$\boldsymbol{\sigma}^* = \boldsymbol{\sigma} - \frac{1}{3}(\mathrm{tr}\boldsymbol{\sigma})\boldsymbol{I} \tag{16}$$

where $\boldsymbol{I}$ is the identity tensor.

In the constitutive equation (15) the stress rate is computed from total stress and strain rate. Apparently the first three terms in Eq. (15) describe the linear behavior of material and the last term describes the non-linear behavior. The constitutive equation is homogeneous of the first degree in stress, which means that the predicted behavior, for example tangential stiffness and shear strength, depends linearly on the stress level. This can be regarded as a reasonable approximation for small to moderate variation of the stress level in soils. The four parameters of the specific constitutive equation (15) are easy to determine. They can be identified with the conventional triaxial test. Alternatively, they can be related to some commonly used parameters in soil mechanics such as tangential stiffness, Poisson ratio, friction angle and dilatancy angle [27]. In this paper the hypoplastic parameters are determined from a single triaxial test, considering two specific stress states, namely, the initial hydrostatic state and the stress state at failure. Four parameters obtained from the triaxial test are used (with $R = \sigma_1/\sigma_3$), i.e. the initial tangential modulus $E_i = [(\dot{\sigma}_1 - \dot{\sigma}_3)/\dot{\varepsilon}_1]_{R=1}$, the

initial Poisson ratio $\nu_i = [\dot{\varepsilon}_3/\dot{\varepsilon}_1]_{R=1}$, the failure stress ratio $R_f = [\sigma_1/\sigma_3]_{\max}$ and the failure Poisson ratio $\nu_f = [\dot{\varepsilon}_3/\dot{\varepsilon}_1]_{R=R_f}$. The failure stress ratio R_f and failure Poisson ratio ν_f can be further related to the well-established parameters friction angle ϕ and dilatancy angle ψ in the following way [27]:

$$R_f = \frac{1+\sin\phi}{1-\sin\phi} \tag{17}$$

$$\nu_f = \frac{1+\tan\psi}{2} \tag{18}$$

As a consequence, the four hypoplastic parameters can be computed from four common parameters: the initial tangent modulus E_i, the initial Poisson ratio ν_i, the friction angle ϕ and the dilatancy angle ψ. It is worth noting that in the context of hypoplasticity the tangential stiffness of material is dependent on the stress state. Therefore, it is necessary to specify the confine pressure σ_3 under which the triaxial test is performed. In this paper all the parameters are assumed to be obtained from triaxial tests with confine pressure σ_3=100 kPa.

The failure surface calculated from constitutive equation (15) is of the Drucker-Prager type [34], which is a cone with its apex at the origin of the co-ordinate system. The performance of the adapted hypoplastic model has been demonstrated in detail in the works by Wu et al [27, 26, 38] and Wang [34], and this model has been implemented in a finite differential code to solve boundary value problems [34, 39].

3.3. Discretization of hypoplastic model in SPH

As the hypoplastic constitutive equation (15) is already in rate form, its discretization in SPH is quite straightforward. For a given particle i the stress-strain relationship can be written as

$$\frac{\mathrm{d}\boldsymbol{\sigma}_i}{\mathrm{d}t} = \dot{\boldsymbol{\omega}}_i\boldsymbol{\sigma}_i - \boldsymbol{\sigma}_i\dot{\boldsymbol{\omega}}_i + c_1(\mathrm{tr}\boldsymbol{\sigma}_i)\dot{\boldsymbol{\varepsilon}}_i + c_2(\mathrm{tr}\dot{\boldsymbol{\varepsilon}}_i)\boldsymbol{\sigma}_i + c_3\frac{\mathrm{tr}(\boldsymbol{\sigma}_i\dot{\boldsymbol{\varepsilon}}_i)}{\mathrm{tr}\boldsymbol{\sigma}_i}\boldsymbol{\sigma}_i + c_4(\boldsymbol{\sigma}_i + \boldsymbol{\sigma}_i^*) \parallel \dot{\boldsymbol{\varepsilon}}_i \parallel \tag{19}$$

where $\boldsymbol{\sigma}_i$, $\dot{\boldsymbol{\varepsilon}}_i$ and $\dot{\boldsymbol{\omega}}_i$ are the stress tensor, strain rate tensor and spin tensor at particle i, respectively. The stress rate tensor is calculated directly from the stress state and strain rate through the above constitutive equation. When applying Eq. (19), it is not required to split strain tensor into elastic part and plastic part. Furthermore, complex stress return mapping usually necessary in elastoplastic models is not needed. Therefore, the hypoplastic model greatly simplifies the numerical implementation in SPH code.

The strain rate and spin tensor at particle i in Eq. (19) are computed from the velocity gradient, which is obtained from the SPH approximation over particles in its support domain by applying Eq. (7)

$$\nabla\boldsymbol{v}_i = \sum_{j=1}^{n}\boldsymbol{v}_j \otimes \nabla_i W_{ij} m_j/\rho_j \tag{20}$$

It is found however, more accurate results can be achieved if the velocity gradient is computed using a symmetric form [8], by taking the velocity difference between two interacting particles into consideration

$$\nabla \boldsymbol{v}_i = \sum_{j=1}^{n} (\boldsymbol{v}_j - \boldsymbol{v}_i) \otimes \nabla_i W_{ij} m_j / \rho_j \tag{21}$$

This gives rise to the following SPH discretized formulations of strain rate tensor and spin tensor

$$\dot{\boldsymbol{\varepsilon}}_i = \frac{1}{2}\left[\left(\sum_{j=1}^{n} (\boldsymbol{v}_j - \boldsymbol{v}_i) \otimes \nabla_i W_{ij} m_j / \rho_j\right) + \left(\sum_{j=1}^{n} (\boldsymbol{v}_j - \boldsymbol{v}_i) \otimes \nabla_i W_{ij} m_j / \rho_j\right)^{\mathrm{T}}\right] \tag{22}$$

$$\dot{\boldsymbol{\omega}}_i = \frac{1}{2}\left[\left(\sum_{j=1}^{n} (\boldsymbol{v}_j - \boldsymbol{v}_i) \otimes \nabla_i W_{ij} m_j / \rho_j\right) - \left(\sum_{j=1}^{n} (\boldsymbol{v}_j - \boldsymbol{v}_i) \otimes \nabla_i W_{ij} m_j / \rho_j\right)^{\mathrm{T}}\right] \tag{23}$$

The hypoplastic equation (15) is mainly developed for cohesionless soils. In practice, however, most soils show cohesion to some extent. The adapted constitutive model is also able to take cohesion into consideration by simply replacing the stress tensor $\boldsymbol{\sigma}$ with the following translated stress tensor [34]

$$\boldsymbol{\eta} = \boldsymbol{\sigma} - c\boldsymbol{I} \tag{24}$$

where c is the cohesion. With this extension, the discretized stress-strain relationship (19) can be rewritten as follows

$$\frac{\mathrm{d}\boldsymbol{\eta}_i}{\mathrm{d}t} = \dot{\boldsymbol{\omega}}_i \boldsymbol{\eta}_i - \boldsymbol{\eta}_i \dot{\boldsymbol{\omega}}_i + c_1(\mathrm{tr}\boldsymbol{\eta}_i)\dot{\boldsymbol{\varepsilon}}_i + c_2(\mathrm{tr}\dot{\boldsymbol{\varepsilon}}_i)\boldsymbol{\eta}_i + c_3 \frac{\mathrm{tr}(\boldsymbol{\eta}_i \dot{\boldsymbol{\varepsilon}}_i)}{\mathrm{tr}\boldsymbol{\eta}_i}\boldsymbol{\eta}_i + c_4(\boldsymbol{\eta}_i + \boldsymbol{\eta}_i^*) \parallel \dot{\boldsymbol{\varepsilon}}_i \parallel \tag{25}$$

where $\boldsymbol{\eta}^*$ is the deviatoric part of the translated stress tensor $\boldsymbol{\eta}$.

4. Numerical implementations

4.1. artificial viscosity and artificial stress

In SPH, to stabilize the numerical scheme and alleviate the unphysical oscillations, a dissipative term is usually incorporated in the momentum equation. The most commonly used form is the artificial viscosity proposed by Monaghan [10]

$$\Pi_{ij} = \begin{cases} \dfrac{-\alpha c_s \phi_{ij} + \beta \phi_{ij}^2}{\bar{\rho}_{ij}}, & \boldsymbol{v}_{ij} \cdot \boldsymbol{r}_{ij} < 0 \\ 0 \qquad\quad , & \boldsymbol{v}_{ij} \cdot \boldsymbol{r}_{ij} \geq 0 \end{cases} \tag{26}$$

with

$$\phi_{ij} = \frac{h \boldsymbol{v}_{ij} \cdot \boldsymbol{r}_{ij}}{\parallel \boldsymbol{r}_{ij} \parallel^2 + 0.01h^2}, \quad \bar{\rho}_{ij} = \frac{\rho_i + \rho_j}{2} \tag{27}$$

where $\boldsymbol{v}_{ij} = \boldsymbol{v}_i - \boldsymbol{v}_j$ and $\boldsymbol{r}_{ij} = \boldsymbol{x}_i - \boldsymbol{x}_j$; c_s is the artificial speed of sound, which will be further specified in Section 4.3. It can be seen that the artificial viscosity consists of two terms: the first term associated with the coefficient α produces a shear and bulk viscosity; the other one, which is associated with coefficient β, is necessary to prevent unphysical particle penetration in very high speed flows. The appropriate values of α and β should be tuned in particular problems.

It is widely reported that SPH suffers from the so called 'tensile instability' problem. That is, when the material is in a state of stretching, the particles tend to form small clumps, which eventually results in unphysical fractures. In material with tensile strength, this tensile instability is usually difficult to detect because it mimics the process of cracking in many situations. Among the remedies developed to alleviate this instability, the artificial stress method [36] is one of the most successful techniques and perhaps the most widely used. This method is an analog to the atomic force, in which a short range repulsive force is added to the momentum equation when the material is in tensile state. As a consequence, the particles are prevented from getting too close to each other. In the artificial stress method the additional stress term has the following form

$$\boldsymbol{S}_{ij} = f_{ij}^n(\boldsymbol{R}_i + \boldsymbol{R}_j) \tag{28}$$

where f_{ij} is defined as $f_{ij} = W_{ij}/W(\Delta p)$ and Δp is the initial particle spacing; the exponential factor n is taken as $n = W(0)/W(\Delta p)$. If a constant ratio $h/\Delta p = 1.2$ is assumed, for cubic spine kernel the repulsive force will increase about 11 times as the distance r between two particles decreases from Δp to 0. The artificial stress drops rapidly in the range $h < r \leq 2h$, which ensures that the correction only takes effect in the nearest neighboring particles.

The term $\boldsymbol{R}_i$ is usually obtained by computing the principal stresses by rotating the Cartesian coordinates [36]. In this paper we use a simplified expression proposed by Xu [40]

$$R_i^{mn} = \begin{cases} \dfrac{-b\sigma_i^{mn}}{\rho_i^2}, & \sigma_i^{mn} > 0 \\ 0 \quad , & \sigma_i^{mn} \leq 0 \end{cases} \tag{29}$$

where R_i^{mn} and σ_i^{mn} are the components of $\boldsymbol{R}_i$ and $\boldsymbol{\sigma}_i$ respectively, m and n denote Cartesian components; b is a positive coefficient. The same method is used to compute $\boldsymbol{R}_j$.

With the corrections of artificial viscosity and artificial stress, the momentum equation Eq. (11) is replaced by

$$\frac{\mathrm{d}\boldsymbol{v}_i}{\mathrm{d}t} = \sum_{j=1}^{n}(\frac{\boldsymbol{\sigma}_i}{\rho_i^2} + \frac{\boldsymbol{\sigma}_j}{\rho_j^2} - \Pi_{ij}\boldsymbol{I} + \boldsymbol{S}_{ij})\nabla_i W_{ij} m_j + \boldsymbol{g}_i \tag{30}$$

4.2. Boundary condition

Boundary condition is one of the key aspects in SPH and special attention should be paid to achieve an accurate representation of them. One of the advantages of SPH is that free surface boundary is satisfied naturally in its formulations. As to wall boundary, however, the SPH method may suffer from the problem of particle deficiency. This particle deficiency is induced when the support domain of a particle intersects with wall boundary, resulting in an underestimated integral interpolation because of the incomplete support domain. Several techniques have been proposed to deal with it, such as repulsive forces [10], ghost particles [13] and dummy particles [11].

In the present work, solid boundary is represented by several (usually three) layers of dummy particles, which either remain fixed or move with pre-described velocities. For each soil particle i, if its support domain intersects with the boundary, the enclosed dummy particles contribute to the SPH formulations of velocity and stress gradient like real soil particles, as shown in Fig 1(a). The velocity of a boundary particle j is directly assigned either zero value or the velocity of the wall boundary v_w, representing the fixed wall condition and the moving boundary condition, respectively. This treatment is a simplification of the method in [18].

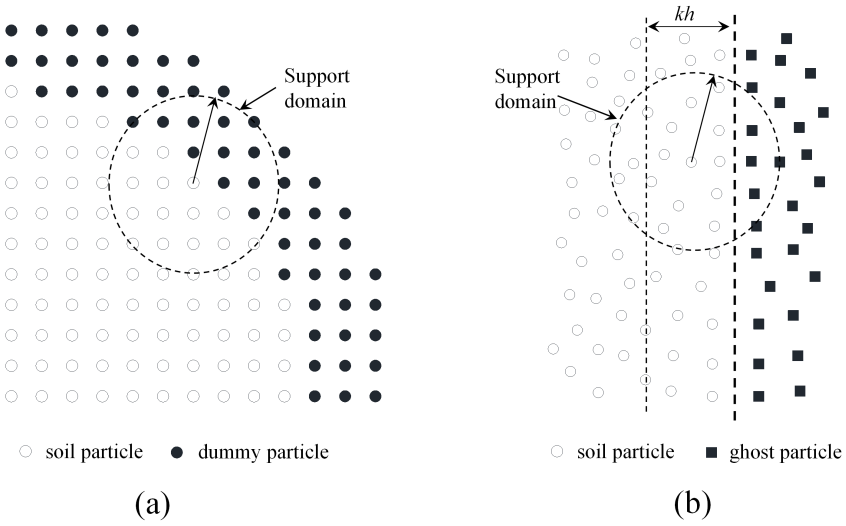

Figure 1: Sketch of two types of solid boundary treatments: (a) dummy particles for non-slip boundary; (b) ghost particles for free-slip boundary.

Apart from velocities, it is also crucial to assign appropriate stress values to the dummy particles. In fluid applications, the pressure at a dummy particle is usually computed from density variation. As fluid particles approaching boundary, the density of a dummy particle increases, resulting in increasing pressure which acts as repulsive force. This approach is incapable of modeling the solid boundary in our application, as the evolution of strains is more complex than density. Bui et al [18] assumes a locally uniform distribution

of stress on the solid boundary. In their treatment, for a given soil particle i, a boundary particle j in its support domain is assigned the same stress tensor as i. In this way, if the soil particle i approaches the boundary, all the interacted boundary particles will have the same stress tensor as the soil particle considered. This treatment gives rise to repulsive forces to prevent soil particles from penetrating the boundary. It is observed in simulations however, that this approach is insufficient to completely avoid particle penetration, especially in problems involving fast particle flow. Through numerical investigation, we found that particles in the state of fast flow usually have very low stress level. In such circumstance, the original boundary treatment results in very small repulsive forces, which are not large enough to push soil particles away from the boundary. Based on this observation, we introduce a minor correction into the original method. That is, all the boundary particles in the support domain of soil particle i are assigned a stress tensor $\boldsymbol{\sigma}_{\max}$, instead of the stress tensor $\boldsymbol{\sigma}_i$. The stress tensor $\boldsymbol{\sigma}_{\max}$ is computed by

$$\sigma_{\max}^{\alpha\alpha} = \min_{k=1}^{n} \sigma_k^{\alpha\alpha} \tag{31}$$

where $\sigma^{\alpha\alpha}$ is the diagonal components of stress tensor; n is the number of *soil particles* in the neighborhood of particle i. The off-diagonal components of $\boldsymbol{\sigma}_{\max}$ are taken as the same as those of $\boldsymbol{\sigma}_i$. Bearing in mind that compression is taken as negative, obviously that Eq. (31) produces a stress tensor in the state of compression with relatively large components. This correction gives rise to large enough repulsive force in boundary particles, thus soil particle penetration can be completely avoided.

The dummy particle method is applied to model non-slip boundary condition. To simulate free-slip boundary condition, ghost particles are used. As demonstrated in Figure 1(b), if a soil particle i is located within a certain distance from the boundary, a corresponding ghost particle is placed symmetrically on the outside of the boundary. The distance is usually taken as kh and in this paper $k = 2$ is used. At a ghost particle, all the variables are assigned the same values as at the real soil particle except the velocity. The velocity tangential to the boundary is kept unchanged as the real soil particle, while the velocity normal to the boundary is taken as minus of the original value. With this treatment, the requirement of free-slip condition can be fulfilled.

4.3. Explicit time integration

In SPH, Eq. (19) and Eq. (30) constitute the complete system of equations for numerical simulation. These equations are solved by integrating in time with a Verlet scheme. In each step, the interactions between pairs of particles are computed, then the variables at each particle are updated using the following explicit integration

$$\boldsymbol{v}_i^{n+1} = \boldsymbol{v}_i^{n-1} + 2\Delta t \left(\frac{\mathrm{d}\boldsymbol{v}_i}{\mathrm{d}t} \right)^n \tag{32}$$

$$\boldsymbol{x}_i^{n+1} = \boldsymbol{x}_i^n + \Delta t \boldsymbol{v}_i^n + 0.5\Delta t^2 \left(\frac{\mathrm{d}\boldsymbol{v}_i}{\mathrm{d}t}\right)^n \tag{33}$$

$$\boldsymbol{\sigma}_i^{n+1} = \boldsymbol{\sigma}_i^{n-1} + 2\Delta t \left(\frac{\mathrm{d}\boldsymbol{\sigma}_i}{\mathrm{d}t}\right)^n \tag{34}$$

$$\boldsymbol{\varepsilon}_i^{n+1} = \boldsymbol{\varepsilon}_i^{n-1} + 2\Delta t \left(\frac{\mathrm{d}\boldsymbol{\varepsilon}_i}{\mathrm{d}t}\right)^n \tag{35}$$

where $n-1$, n and $n+1$ denote the time steps. With Verlet scheme the interactions between particles are computed only once per step. In addition, all the variables are computed at time steps, not half time steps as in a Leap-Frog integration. This property is helpful for achieving a simple implementation of the time integration. Similar to other explicit integration schemes, Verlet integration requires a sufficiently small time step for stability reasons. A variable time step Δt is calculated using the common CFL condition and the acceleration term [11]

$$\Delta t_1 = \min_i(\sqrt{h/ \parallel \boldsymbol{a}_i \parallel}) \tag{36}$$

$$\Delta t = \chi_{CFL}\min(\Delta t_1, h/c_s) \tag{37}$$

where $\boldsymbol{a}_i$ is the acceleration of particle i; χ_{CFL} is the CFL number and c_s is the artificial speed of sound. In this work the artificial speed of sound c_s is taken as 100 m/s and CFL number $\chi_{CFL} = 0.05$ is applied. This will generate a sufficiently small time step thus the stability of computation can be guaranteed.

5. Numerical examples

In this section, three problems are numerically simulated to demonstrate the performance of the proposed method. In all simulations, the problem domain is discretized with particles in a regular lattice in which the particle spacing is Δp. The smoothing length h is fixed as $h/\Delta p = \sqrt{2}$ in the computations. The coefficients of artificial viscosity are chosen by numerical tests, and we find that $\alpha = 1.0$ and $\beta = 0.1$ give rise to stable and reasonable results in all our simulations. The coefficient of artificial stress is taken as $b = 0.3$ and only applied in the slope stability case. Although the continuity equation is not taken into consideration, a reference density is necessary in the SPH formulations. In this paper $\rho_0 = 1850$ kg/m^3 is used. The material parameters used in following simulations are listed in Table 1.

Table 1. Material parameters used in numerical examples.

Numerical test	Material constants					Hypoplastic parameters			
	E_i [MPa]	ν_i [-]	ϕ [°]	ψ [°]	c [kPa]	c_1 [-]	c_2 [-]	c_3 [-]	c_4 [-]
Oedometer test	21.0	0.2	29.5	1.0	0.0	-58.3	-178.5	-589.0	-182.7
Sand collapse	20.0	0.2	30.0	1.0	0.0	-55.6	-171.2	-540.9	-170.9
Slope stability	30.0	0.2	30.0	0.0	5.0	-83.3	-264.9	-781.3	-255.2

5.1. Oedometer test

An oedometer test with confined radial deformation is considered. The oedometer test has quite simple boundary conditions, thus analytical solutions can be readily obtained. As a result, it is selected to validate the implementation of the hypoplastic constitutive model, as well as the whole SPH application.

The simulation is performed under plain-strain condition. A total number of 5000 soil particles are used to represent an soil column 1 m in height and 0.5 m in width. As shown in Figure 2, the vertical free-slip boundaries are modeled by ghost particles. The non-slip boundary condition is applied to the bottom and top cover, which are modeled with dummy particles. In the simulation, the bottom is fixed, while the top cover moves vertically to reproduce the loading condition. The simulated soil is a cohesionless sand. Material constants and hypoplastic parameters are given in Table 1. Within the framework of hypoplasticity, computation cannot start from zero stress level. Therefore, a small hydrostatic pressure $-p$ is assigned to the soil particles as initial stress. The weight of soil is not considered so the gravity is set to zero. The computation includes the first loading and the subsequent unloading, which are performed by moving the top cover downwards and upwards. From the viewpoint of hypoplastic constitutive model, the loading speed is arbitrary since the constitutive equation Eq. (15) is rate-independent. But for the stability and accuracy of the SPH computation, the simulation are carried out with a very small loading speed of 1 cm/s.

Figure 3 presents a comparison between numerical results and analytical solutions obtained with two different initial stress levels. In numerical results, the strains are obtained through dividing the displacement of the top boundary by the sample height, and stresses by averaging the forces acting on the top boundary over the cross-area. The analytical solution is obtained by integrating the constitutive equation (15) [27], with the same boundary conditions. It can be seen that in general the SPH results agree well with the analytical solutions. The axial tangential stiffness increases gradually along with the loading. From loading to unloading the drastic change of axial tangential stiffness is well captured. Also, the compressibility varies with initial stress: starting from a higher initial stress level, the axial tangential stiffness is larger, and the sand is less compressible. From Figure 3(a) it can also be noted that in the loading process, the simulations give exact results as analytical solutions; while in the unloading phase, the stresses from numerical solution are observed to decrease slightly more quickly than they should be. This slight difference may result from

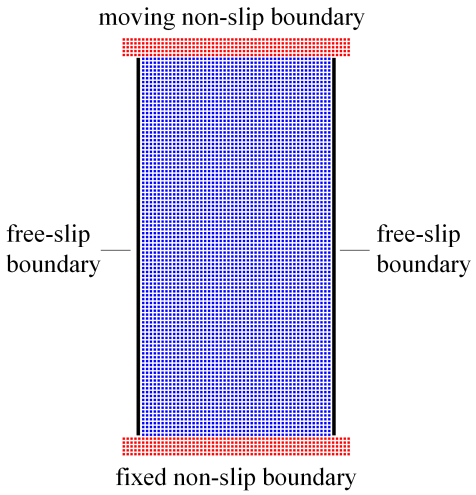

Figure 2: Model of the oedometer test and the boundary conditions.

the implementation of boundary condition of the top cover.

The earth pressure at rest $K_0 = \sigma_3/\sigma_1$ is an important parameter in many geotechnical engineering problems. As may be seen from Figure 3(b), in loading the stress path is a straight line, indicating a constant K_0. The value of K_0 in loading is about 0.51 according to the figure. Analytically, Wu and Bauer gave a method to calculate the K_0 using the parameters c_i (i=1, ..., 4) in the hypoplastic constitutive model proposed in [27]. With a similar procedure, the following algebraic equation is formulated to calculate the K_0 in the oedometer test when constitutive equation (15) is used

$$(6c_1 + 2c_4)K_0^2 + (3c_1 - c_4)K_0 - c_4 = 0 \tag{38}$$

Substituting the parameters c_i (i=1, ..., 4) into the equation above and solving it, we obtain $K_0 = 0.5109$, which is in good agreement with the SPH simulation. Note that in unloading the axial stresses decrease more rapidly than the radial stress, which gives rise to an increase of K_0. This observation is well corroborated by experimental results on soils [41]. The comparison between numerical results and analytical solutions shows that the SPH gives generally accurate results.

5.2. Collapse of sand

The collapse of granular material on a flat surface has been studied experimentally and numerically [21, 42, 43, 44]. This problem with well defined initial and boundary condition is helpful for understanding the physics of gravity-driven granular flow. Moreover, it serves also as a benchmark for numerical methods. In this section, the capacity of the proposed SPH approach is examined by comparing the simulation with the experiment data.

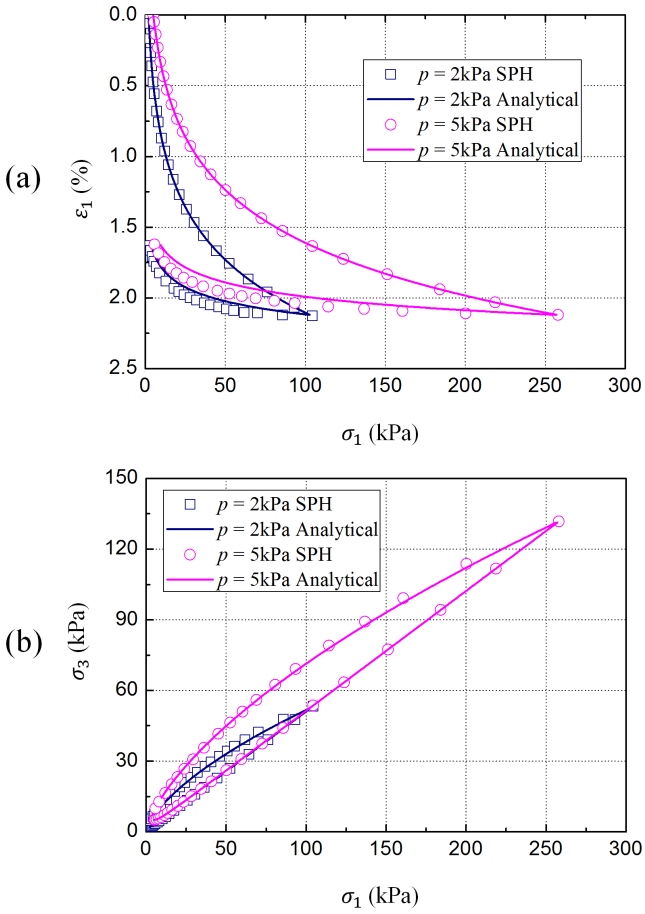

Figure 3: Comparison of numerical results and analytical solutions on oedometer test at different initial stress levels: (a) axial strain vs. axial stress; (b) radial stress vs. axial stress.

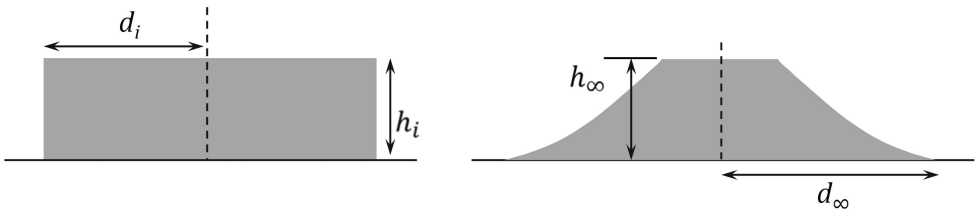

Figure 4: The geometry of initial configuration and final deposit in sand collapse problem.

There are two kinds of set-up of the experiment: axisymmetric [42] and two-dimensional [43]. The two-dimensional experiment is simulated in this work. The set-up of the problem is shown in Figure 4. A rectangle of sand between two parallel plates is confined by gates and remains static. During experiment

the gates are opened and the sand is released. As shown in previous studies, the aspect ratio $a = h_i/d_i$ determines the collapse mode. Following the set-up in Figure 4, a two-dimensional simulation has been performed under plain strain condition. Initially a K_0 stress state is assigned to the particles of the granular at rest. Non-slip boundary condition is applied to model the bottom surface by using dummy particles. The problem is simulated numerically by applying gravity loading and then marching forward in time. In the simulation the initial particle spacing is $\Delta p = 2$ mm and the initial width is $d_i = 0.2$ m. Previous numerical investigations [21, 44] are mainly focused on the influence of aspect ratio a on the mode of collapse process. In this work, our major aim is to validate the numerical approach. To this end, the simulation is carried out on a single aspect ratio $a = 0.5$, which is in the *low aspect* range according to previous experiments [43]. As a consequence, the initial height h_i is 0.1 m. The number of the soil particle used in the simulation is about 10000. The hypoplastic parameters and corresponding material constants are given in Table 1. This chosen material property corresponds to the sand in the experiments by Lube et al [43].

Figure 5 shows the simulated profile of the sand sample at different times after the release. It can be seen that the large deformation and moving free surface are well described in the simulation. The simulated collapsing agrees well with the collapse process in the experiment with the same aspect ratio [43]. At first there is a discontinuity in the collapse surface. After a while this discontinuity disappears and a parabolic surface is formed. There exists a slip plane above which the particles move and below which particles are generally at rest. In the final deposit a parabolic surface profile is obtained. The apparent angle of repose is less than the friction angle ϕ of the material. However, the maximum inclination, which is observed near the top of the slope, is estimated to be approximately equal to the friction angle. This phenomenon is also found by other researchers in experiments [18, 43] and numerical simulations [18, 44]. According to the experiments [43], for $a < 1.8$, the final run-out d_∞ can be estimated through $(d_\infty - d_i)/d_i = 1.6a$. For the set-up in our simulation the run-out according to this simple relationship is about 36 cm. The run-out obtained from numerical simulation, however, is about 40 cm. This discrepancy has also been reported by Chen and Qiu [21], who also provided an explanation for it. While the simulation is obtained with a two dimensional model, the real behavior is three dimensional. Nevertheless, our SPH simulation gives rise to smaller discrepancy than the two dimensional simulation in [21].

The performance of different boundary treatment methods is also investigated. Figure 6 presents the simulation results using different methods to assign stresses to the boundary particles. Results in Figure 6(a) is obtained by using our boundary treatment presented in Section 4.2, while results in Figure 6(b) is obtained by using the boundary treatment in [18]. Note that there is no particle penetration when the $\boldsymbol{\sigma}_{\max}$ correction is applied. On the other hand, the original treatment of boundary gives rise to particle penetration. Moreover, the penetrating particles disturb the movement of other nearby soil particles, which pollutes the computation in the neighboring area and results in highly disordered particle distribution. As can be seen in Figure 6(a), the new technique gives rise to a relatively uniform particle distribution near the

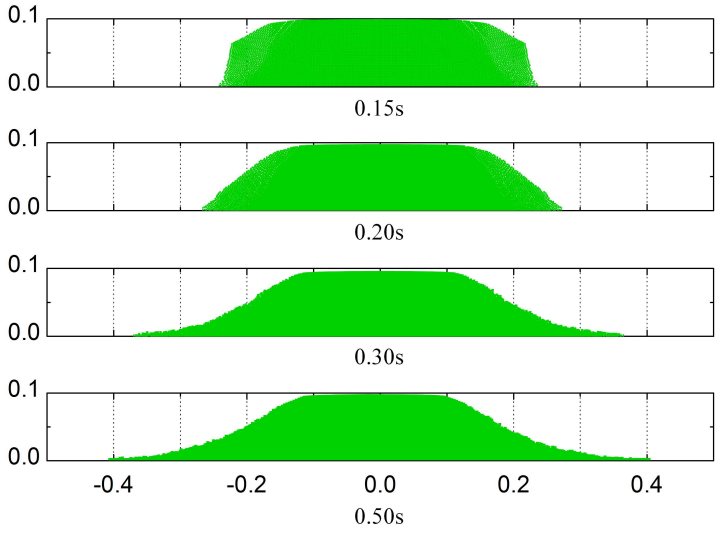

Figure 5: Collapse process of sand with aspect ratio a=0.5 (unit: m).

boundary, which means that more accurate simulations can be achieved.

The stress and strain distributions in the final deposit are shown in Figure 7. The horizontal and vertical stresses increase almost linearly with depth, and are consistent with stresses in a confined column of sand subjected to gravity. Along the center line, the stresses are identical to the initial values before collapse, owing to the fact that the height in this area is not changed in the computation. Regarding the shear stress, there are two areas with relatively large value, locating near the initial toes. This is also expected, because the materials at the toes tend to move side-wards but are confined by the non-slip boundary, hence shear stresses develop in these areas.

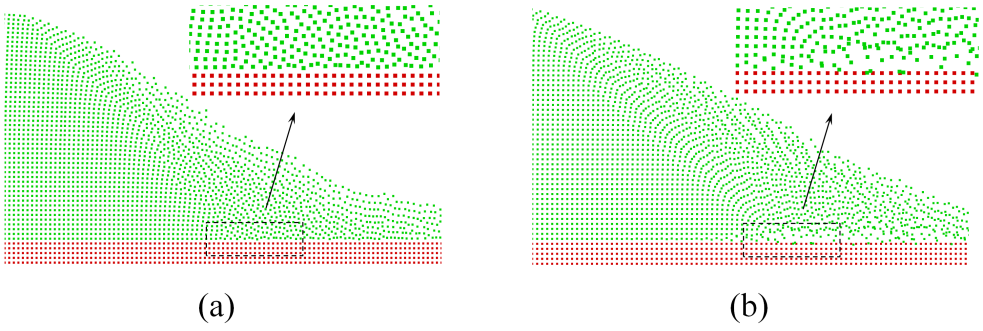

Figure 6: Comparison of boundary treatment methods: (a) boundary particle with stress tensor $\boldsymbol{\sigma}_{\max}$; (b) boundary particle with the same stress tensor as the considered soil particle.

To illustrate the deformation pattern, the equivalent strain $\varepsilon_{\text{eq}} = \sqrt{2/3\boldsymbol{\epsilon}^* : \boldsymbol{\epsilon}^*}$ is plotted in Figure 7(d), where $\boldsymbol{\epsilon}^*$ is the accumulated deviatoric strain defined as $\boldsymbol{\epsilon}^* = \boldsymbol{\epsilon} - (\text{tr}\boldsymbol{\epsilon}/3)\boldsymbol{I}$. It can be seen that the trapezoid region in the middle is undeformed. The collapse occurs along a failure surface above which particles flow

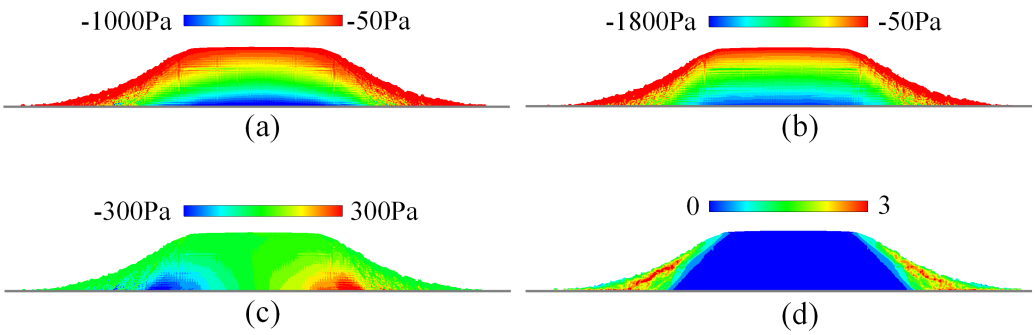

Figure 7: Stresses and equivalent strain at final deposit: (a) horizontal stress σ_{xx}; (b) vertical stress σ_{zz}; (c) shear stress σ_{xz}; (d) equivalent strain ε_{eq}.

down, and below which particles remain at rest. In experiments [43], this failure surface is observed to start from d_i at the bottom with an inclination of about 61° to the horizontal at the early stage of the collapse. The inclination of the failure surface deceases as the collapse develops in experiments, however, the final inclination is not given there. This flow pattern can also be observed in numerical simulation. The distribution of particles at the right part of the sand sample at $t = 0.05$ s in the simulation is shown in Figure 8, where a discontinuity point on the upper surface can be clearly observed. The inclination of the line connecting this discontinuity and the initial toe is about 65°. Below this line the particles remain at rest except some particles near the bottom. This failure line gradually propagates towards the left during the simulation and eventually reaches its final position, which has an inclination of about 45°. This failure mechanism is qualitatively corroborated by the experiments.

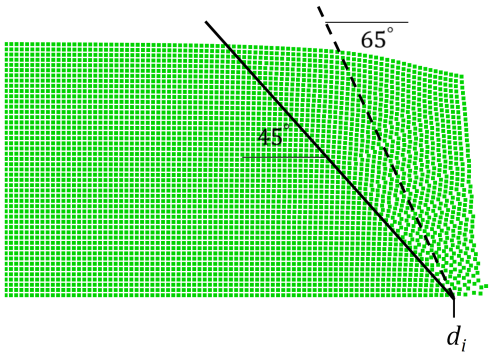

Figure 8: Right part of the sand body at $t = 0.05$ s with initial failure surface (dash line) and final failure surface.

5.3. Safety factor and failure of a homogeneous slope

The proposed method is further validated by evaluating the safety factor of a homogeneous slope and simulating the subsequent failure process. In slope stability analysis, the so called shear strength reduction

technique is usually applied to evaluate the safety [45]. In the strength reduction technique, the shear strength (friction angle and cohesion) is reduced by a reduction factor until slope failure occurs. The safety factor is defined by this reduction factor. Usually, a systematic search is performed to find the reduced shear strength at which slope failure occurs, most commonly with FEM. In this section, the proposed SPH approach is applied to search for the safety factor. Afterwards, we look at the post-failure movement. Results from SPH with hypoplastic and elastoplastic models and FEM with elastoplastic model are compared.

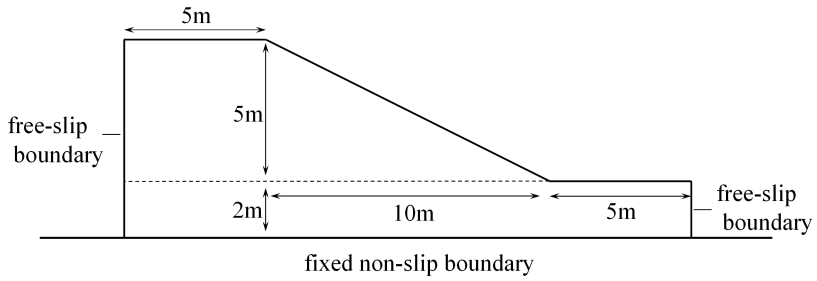

Figure 9: Geometry and boundary conditions of the slope.

The geometry and boundary condition of the considered slope is shown in Figure 9. The slope is assumed to consist of cohesive soil with the material parameters listed in Table 1. The friction angle ϕ and the cohesion c are the two shear strength parameters subjected to strength reduction. In the searching process, the actual shear strength is reduced by a factor f, i.e.

$$c_f = c/f \tag{39}$$

$$\phi_f = \phi/f \tag{40}$$

The reduced shear strength parameters are then used to compute the corresponding hypoplastic parameters by the procedure given in [27]. Note that the failure criterion used in FEM does not apply here, because SPH simulation can always continue at any reduction factor. We proceed to defined the initiation of slope failure by looking at the maximum displacement during a specified time duration [19]. If under a reduction factor the slope keeps stable, the maximum displacement should remain unchanged at a relatively small value after a initial increase. On the other hand, if failure develops, the maximum displacement cannot converge to a small and stable value.

To start with, we employ a rough and straightforward search scheme. Starting from 1.0, the reduction factor f is increased by a step size of 0.1 in each calculation, which corresponds to a real time step of 0.5 second. If the maximum displacement remains small and stable in this time step we move to the next calculation with an increased reduction factor, until finally a large increase of maximum displacement is observed, which means the point of failure is reached. As a result, the reduction factor applied in the last

computation is assumed to be the safety factor. It is worth noting that the failure criterion in SPH is not clearly defined as that in the FEM. There still calls for more objective failure criterion.

The considered slope is discretized by 9000 particles placed in a lattice with particle spacing $\Delta p = 0.1$ m. As the problem is solved dynamically in SPH, the initial condition is very important for the numerical simulation. The soil self-weight is applied by gravity loading [20]. With the help of a damping term, the stress fluctuations induced by the abruptly enforcing of gravity dissipate with time, and the particles eventually reach an equilibrium state. The original (unreduced) shear parameters are used when computing the initial stresses. Figure 10 presents the distribution of the initial stresses by gravity loading. The stress distributions are similar to the results obtained by FEM through static loading, which is not shown here. The stresses in Figure 10 are used as initial stresses for all calculations.

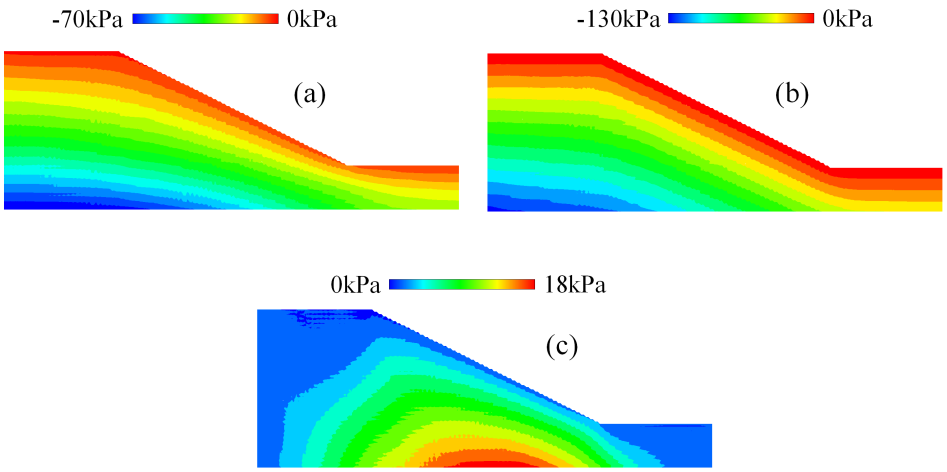

Figure 10: Distribution of initial stresses obtained through SPH: (a) horizontal stress σ_{xx}; vertical stress σ_{zz}; (c) shear stress σ_{xz}.

First a SPH simulation with hypoplastic model is performed. The above described searching procedure is performed, and the safety factor f_s of the slope is found to be 1.9. This means that the slope becomes unstable for the shear parameters of $\phi = 15.8°$ and $c = 2.63$ kPa. Figure 11 shows the development of maximum displacement with time under different reduction factor f. For $f = 1.8$ the maximum displacement of the particle system remains very small, while a rapid increase of displacement is observed after some time when the reduction factor f is 1.9, indicating the initiation of slope failure. For reduction factors larger than 1.9, e.g. 2.0, the maximum displacement increases even more quickly. Obviously, a more accurate safety factor between 1.8 and 1.9 can be obtained if the step size is refined. The failure process depicted by equivalent strain is shown in Figure 12. The propagation of the shear band from the crest to the toe of the slope can be clearly observed. The progressive failure process is well captured by the SPH. In the SPH calculations the thickness of shear band is mainly dictated by the particle spacing Δp and smoothing length h. For

real-world problems however the shear band thickness is an intrinsic material property [46, 47, 48]. In the FEM, the thickness of shear band is modeled by either higher order constitutive equation [49], re-meshing [50] or embedded discontinuity [51].

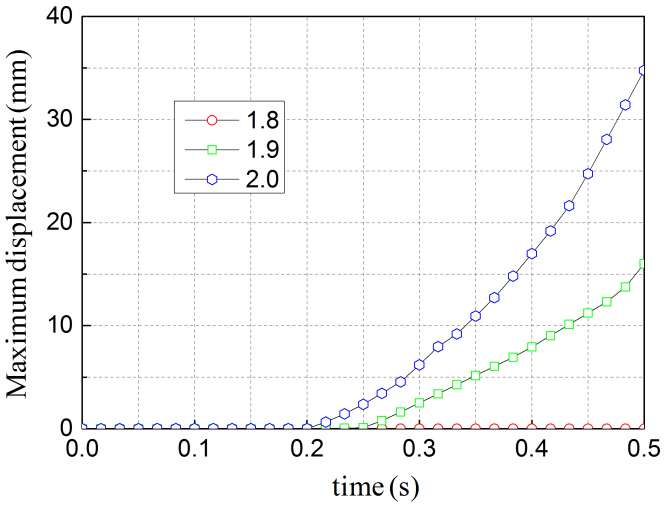

Figure 11: Change of maximum displacement under different reduction factors.

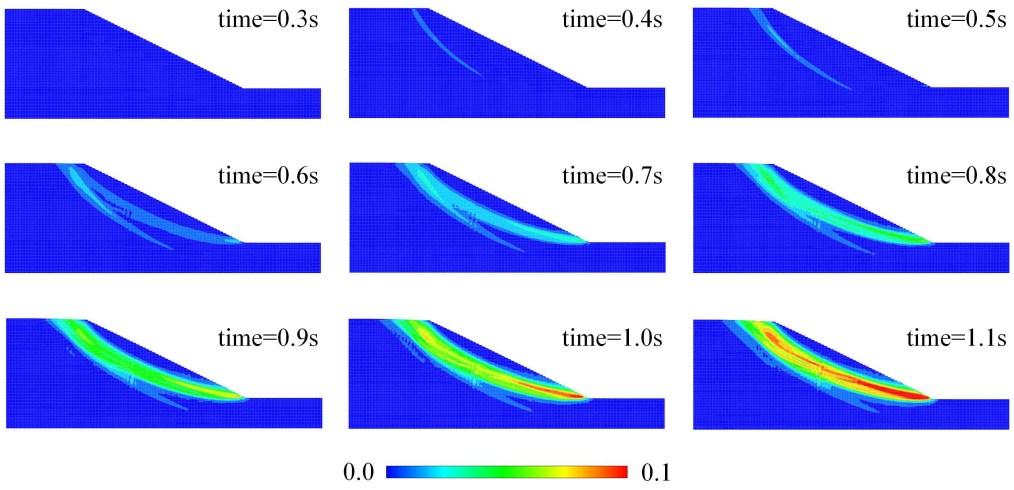

Figure 12: Development of failure surface depicted by total equivalent strain with reduction factor f=1.9.

Using the same geometry and boundary conditions, a SPH simulation with Drucker-Prager (D-P) elsato-plastic model is performed. Our implementation of the D-P model follows the method proposed by Bui et al [19]. The obtained safety factor is 2.0, suggesting a safety factor between 1.9 and 2.0 if refined search is performed. The progressive failure modes in the two SPH simulations are similar. With the same material

constants, a safety factor f_s=1.94 is obtained by FEM with the D-P model. The FEM result is in good agreement with SPH result using the D-P model, while produces a larger safety factor than that obtained using hypoplastic model. The failure surfaces obtained from the three simulations are given in Figure 13. It can be observed that the hypoplastic model gives rise to shallower failure surface and smaller slide body than that given by the D-P model, while the failure surfaces obtained from SPH and FEM using the D-P model are almost the same.

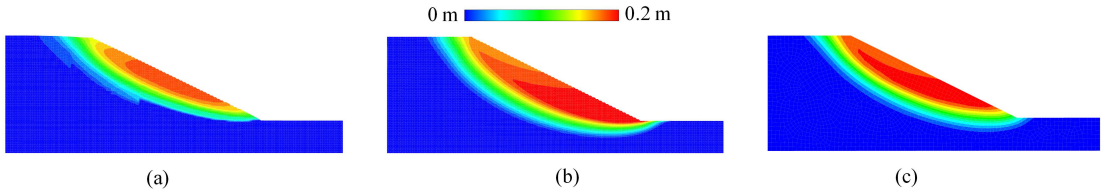

Figure 13: Failure surface depicted by total displacement (a) SPH with hypoplastic model; (b) SPH with D-P model; (c) FEM with D-P model. Note that the colored legend only applies to the SPH results, because the FEM simulation cannot give rise to such large displacement.

For problems with large deformation, however, SPH has definite advantage over FEM. This can be demonstrated by looking at the post failure movement of the slope. A SPH simulation with the hypoplastic model under the reduction factor of 1.9 is performed to model the whole failure process of the slope from the failure initiation to fully developed flow. The evolution of slope failure follows similar pattern as in Figure 12. The slope shows progressive failure with shear band starting from the slope crest and propagating to the slope toe. Once a continuous slip surface is formed, the soil mass above the slip surface slumps downwards until a new equilibrium position is reached. The slope slump is usually characterized by large deformation. Figure 14 shows the slope slump from the SPH calculation, together with the original profile of the slope. The large deformation seems reasonably captured by the SPH method. If an equilibrium position cannot be reached immediately after slumping, slope failure may further develop to debris flow. In this case, the SPH offers an appealing alternative to the FEM to avoid excessively skewed mesh.

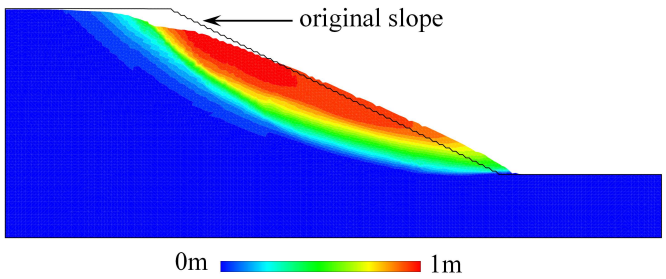

Figure 14: Total displacement and final deposit of the slope after failure.

6. Conclusions

We have implemented a hypoplastic constitutive model in a SPH code for the first time. The hypoplastic model is characterized by its simple formulation and few parameters. The fact that the model is formulated in rate form without decomposing the strain rate into elastic and plastic part renders itself particularly appealing for numerical implementation. The SPH code is validated by three boundary value problems, where the numerical results from SPH are compared with analytical solution, experimental data and the FEM. For problems with large deformation the SPH offers an attractive alternative approach to the FEM. However, the scale problem, e.g. the thickness of shear band, which gives rise to spurious mesh dependence in conventional FEM, remains to be addressed in the SPH. In principle, this can be resolved by choosing appropriate particle space Δp and smoothing length h, which has in turn impact on the computational time. A further issue is concerned with the time scale. For problems of slope failure, the time in the post failure analysis is mainly dictated by gravitation. For problems with large deformation, e.g. debris flow, the viscous behavior need be considered in the run-out analysis. The relevant research is ongoing and the result will be reported in a forthcoming publication.

Acknowledgement

The authors acknowledge the funding from the European Commission under its People Programme (Marie Curie Actions) of the Seventh Framework Programme FP7/2007-2013/ under Research Executive Agency grant agreement no. 289911 under title: Multiscale Modelling of Landslides and Debris Flows. The first author wishes to acknowledge the financial support from the Otto Pregl Foundation for Fundamental Geotechnical Research in Vienna.

References

[1] K J Bathe, E Ramm, and E L Wilson. Finite element formulations for large deformation dynamic analysis. *International Journal for Numerical Methods in Engineering*, 9(2):353–386, 1975.

[2] S Ghosh and N Kikuchi. An arbitrary lagrangian-eulerian finite element method for large deformation analysis of elastic-viscoplastic solids. *Computer Methods in Applied Mechanics and Engineering*, 86(2):127–188, 1991.

[3] Y Hu and M F Randolph. A practical numerical approach for large deformation problems in soil. *International Journal for Numerical and Analytical Methods in Geomechanics*, 22(5):327–350, 1998.

[4] T Rabczuk and T Belytschko. A three-dimensional large deformation meshfree method for arbitrary evolving cracks. *Computer Methods in Applied Mechanics and Engineering*, 196(29):2777–2799, 2007.

[5] C Peng, W Wu, and B Y Zhang. Three-dimensional simulations of tensile cracks in geomaterials by coupling meshless and finite element method. *International Journal for Numerical and Analytical Methods in Geomechanics*, 39(2):135–154, 2015.

[6] W C Sun, M R Kuhn, and J W Rudnicki. A multiscale dem-lbm analysis on permeability evolutions inside a dilatant shear band. *Acta Geotechnica*, 8(5):465–480, 2013.

[7] C T Wu, J S Chen, L Chi, and F Huck. Lagrangian meshfree formulation for analysis of geotechnical materials. *Journal of engineering mechanics*, 127(5):440–449, 2001.

[8] J J Monaghan. Smoothed particle hydrodynamics. *Annual review of astronomy and astrophysics*, 30:543–574, 1992.

[9] V Springel. Smoothed particle hydrodynamics in astrophysics. *Annual Review of Astronomy and Astrophysics*, 48:391–430, 2010.

[10] J J Monaghan. Simulating free surface flows with sph. *Journal of computational physics*, 110(2):399–406, 1994.

[11] M Gomez-Gesteira, B D Rogers, R A Dalrymple, and A J C Crespo. State-of-the-art of classical sph for free-surface flows. *Journal of Hydraulic Research*, 48(S1):6–27, 2010.

[12] A Colagrossi and M Landrini. Numerical simulation of interfacial flows by smoothed particle hydrodynamics. *Journal of Computational Physics*, 191(2):448–475, 2003.

[13] L D Libersky, A G Petschek, T C Carney, J. R. Hipp, and F. A. Allahdadi. High strain lagrangian hydrodynamics: A three-dimensional sph code for dynamic material response. *Journal of Computational Physics*, 109(1):67 – 75, 1993.

[14] G R Johnson, R A Stryk, and S R Beissel. Sph for high velocity impact computations. *Computer methods in applied mechanics and engineering*, 139(1):347–373, 1996.

[15] M B Liu, G R Liu, Z Zong, and K Y Lam. Computer simulation of high explosive explosion using smoothed particle hydrodynamics methodology. *Computers & Fluids*, 32(3):305–322, 2003.

[16] M Pastor, B Haddad, G Sorbino, S Cuomo, and V Drempetic. A depth-integrated, coupled sph model for flow-like landslides and related phenomena. *International Journal for Numerical and Analytical Methods in Geomechanics*, 33(2):143–172, 2009.

[17] H Zhu, N S Martys, C Ferraris, and D D Kee. A numerical study of the flow of bingham-like fluids in two-dimensional vane and cylinder rheometers using a smoothed particle hydrodynamics (sph) based method. *Journal of Non-Newtonian Fluid Mechanics*, 165(7):362–375, 2010.

[18] H H Bui, R Fukagawa, K Sako, and S Ohno. Lagrangian meshfree particles method (sph) for large deformation and failure flows of geomaterial using elastic–plastic soil constitutive model. *International Journal for Numerical and Analytical Methods in Geomechanics*, 32(12):1537–1570, 2008.

[19] HH Bui, Ryoichi Fukagawa, Kazunari Sako, and JC Wells. Slope stability analysis and discontinuous slope failure simulation by elasto-plastic smoothed particle hydrodynamics (sph). *Geotechnique*, 61(7):565–574, 2010.

[20] H H Bui and R Fukagawa. An improved sph method for saturated soils and its application to investigate the mechanisms of embankment failure: Case of hydrostatic pore-water pressure. *International Journal for Numerical and Analytical Methods in Geomechanics*, 37(1):31–50, 2013.

[21] W Chen and T Qiu. Numerical simulations for large deformation of granular materials using smoothed particle hydrodynamics method. *International Journal of Geomechanics*, 12(2):127–135, 2011.

[22] J Wang and D Chan. Frictional contact algorithms in sph for the simulation of soil–structure interaction. *International Journal for Numerical and Analytical Methods in Geomechanics*, 38(7):747–770, 2014.

[23] D Kolymbas. An outline of hypoplasticity. *Archive of applied mechanics*, 61(3):143–151, 1991.

[24] W Wu, E Bauer, and D Kolymbas. Hypoplastic constitutive model with critical state for granular materials. *Mechanics of materials*, 23(1):45–69, 1996.

[25] G. Gudenhus. A comprehensive equation for granular materials. *Soil and foundations*, 36(1):1–12, 1996.

[26] W Wu and A Niemunis. Failure criterion, flow rule and dissipation function derived from hypoplasticity. *Mechanics of Cohesive-frictional Materials*, 1(2):145–163, 1996.

[27] W Wu and E Bauer. A simple hypoplastic constitutive model for sand. *International Journal for Numerical and Analytical Methods in Geomechanics*, 18(12):833–862, 1994.

[28] P A von Wolffersdorff. A hypoplastic relation for granular materials with a predefined limit state surface. *Mechanics of*

Cohesive-frictional Materials, 1(3):251–271, 1996.

[29] D Mašín. A hypoplastic constitutive model for clays. *International Journal for Numerical and Analytical Methods in Geomechanics*, 29(4):311–336, 2005.

[30] J Tejchman and E Bauer. Numerical simulation of shear band formation with a polar hypoplastic constitutive model. *Computers and Geotechnics*, 19(3):221–244, 1996.

[31] V A Osinov, S Chrisopoulos, and T Triantafyllidis. Numerical study of the deformation of saturated soil in the vicinity of a vibrating pile. *Acta Geotechnica*, 8(4):439–446, 2013.

[32] J Hleibieh, D Wegener, and I Herle. Numerical simulation of a tunnel surrounded by sand under earthquake using a hypoplastic model. *Acta Geotechnica*, 9(4):631–640, 2014.

[33] C Fang and W Wu. On the weak turbulent motions of an isothermal dry granular dense flow with incompressible grains: part ii. complete closure models and numerical simulations. *Acta Geotechnica*, 9(5):739–752, 2014.

[34] X T Wang and W Wu. An updated hypoplastic constitutive model, its implementation and application. In *Bifurcations, Instabilities and Degradations in Geomaterials*, pages 133–143. Springer, 2011.

[35] J J Monaghan. An introduction to sph. *Computer physics communications*, 48(1):89–96, 1988.

[36] J P Gray, J JJ Monaghan, and R P Swift. Sph elastic dynamics. *Computer methods in applied mechanics and engineering*, 190(49):6641–6662, 2001.

[37] W Wu and D Kolymbas. Numerical testing of the stability criterion for hypoplastic constitutive equations. *Mechanics of materials*, 9(3):245–253, 1990.

[38] W Wu and D Kolymbas. Hypoplasticity then and now. In *Constitutive modelling of granular materials*, pages 57–105. Springer, 2000.

[39] X T Wang. *An updated hypoplastic model, its implementation, and its application in tunnelling*. PhD thesis, University of Natural Resources and Applied Life Sciences, Vienna, 2009.

[40] X Y Xu, J Ouyang, B X Yang, and Z J Liu. Sph simulations of three-dimensional non-newtonian free surface flows. *Computer Methods in Applied Mechanics and Engineering*, 256:101–116, 2013.

[41] P W Mayne and F H Kulhawy. K0-ocr relationships in soil. *Journal of the Geotechnical Engineering Division*, 108(6):851–872, 1982.

[42] G Lube, H E Huppert, R S J Sparks, and M A Hallworth. Axisymmetric collapses of granular columns. *Journal of Fluid Mechanics*, 508:175–199, 2004.

[43] G Lube, H E Huppert, R S J Sparks, and A Freundt. Collapses of two-dimensional granular columns. *Physical Review E*, 72(4):041301, 2005.

[44] C M Mast, P Arduino, P Mackenzie-Helnwein, and G R Miller. Simulating granular column collapse using the material point method. *Acta Geotechnica*, pages 1–16, 2014.

[45] D V Griffiths and P A Lane. Slope stability analysis by finite elements. *Geotechnique*, 49(3):387–403, 1999.

[46] L Zhuang, Y Nakata, U Kim, and D Kim. Influence of relative density, particle shape, and stress path on the plane strain compression behavior of granular materials. *Acta Geotechnica*, 9(2):241–255, 2014.

[47] H M Zbib and E C Aifantis. On the structure and width of shear bands. *Scripta metallurgica*, 22(5):703–708, 1988.

[48] A S Gylland, H P Jostad, and S Nordal. Experimental study of strain localization in sensitive clays. *Acta Geotechnica*, 9(2):227–240, 2014.

[49] J Tejchman and W Wu. Dynamic patterning of shear bands in cosserat continuum. *Journal of engineering mechanics*, 123(2):123–133, 1997.

[50] A R Khoei, A R Tabarraie, and S A Gharehbaghi. H-adaptive mesh refinement for shear band localization in elasto-plasticity cosserat continuum. *Communications in Nonlinear Science and Numerical Simulation*, 10(3):253–286, 2005.

[51] C D Foster and T M Nejad. Embedded discontinuity finite element modeling of fluid flow in fractured porous media. *Acta*

Geotechnica, 8(1):49–57, 2013.